On the interaction of Tollmien-Schlichting waves with a wall-embedded Helmholtz resonator

Michelis, T.; De Koning, C.; Kotsonis, M.

DOI
10.1063/5.0141685

Publication date
2023

Document Version
Final published version

Published in
Physics of Fluids

Citation (APA)
Michelis, T., De Koning, C., & Kotsonis, M. (2023). On the interaction of Tollmien-Schlichting waves with a wall-embedded Helmholtz resonator. *Physics of Fluids*, *35*(3), Article 034104. https://doi.org/10.1063/5.0141685

Physics of Fluids

On the interaction of Tollmien–Schlichting waves with a wall-embedded Helmholtz resonator

Cite as: Phys. Fluids **35**, 034104 (2023); https://doi.org/10.1063/5.0141685
Submitted: 07 January 2023 • Accepted: 13 February 2023 • Published Online: 06 March 2023

T. Michelis, C. de Koning and M. Kotsonis

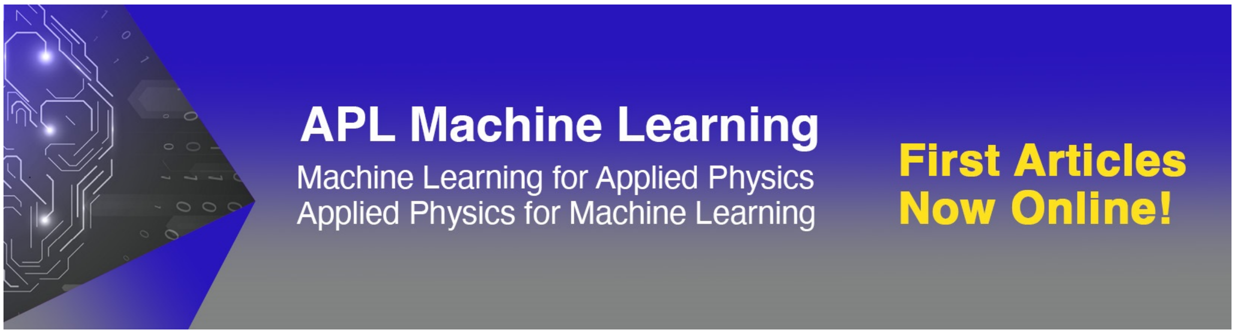

AIP Publishing

Phys. Fluids **35**, 034104 (2023); https://doi.org/10.1063/5.0141685 **35**, 034104

Physics of Fluids ARTICLE scitation.org/journal/phf

On the interaction of Tollmien–Schlichting waves with a wall-embedded Helmholtz resonator

Cite as: Phys. Fluids **35**, 034104 (2023); doi: 10.1063/5.0141685
Submitted: 7 January 2023 · Accepted: 13 February 2023 ·
Published Online: 6 March 2023

T. Michelis,[a] C. de Koning, and M. Kotsonis

AFFILIATIONS

Faculty of Aerospace Engineering, Delft University of Technology, Kluyverweg 1, 2629HS Delft, The Netherlands

[a]Author to whom correspondence should be addressed: t.michelis@tudelft.nl

ABSTRACT

The influence of a wall-embedded Helmholtz resonator on the development and stability of Tollmien–Schlichting (TS) waves is investigated numerically and experimentally for a range of frequencies extending from below to above resonance. Interactions are found to be limited in the near-wall region and toward the trailing edge of the resonator orifice while at the same time being linear nature. The dynamic response of the flow-excited resonator is shown to have a fixed phase relation with respect to the TS-waves, indicating that only amplification of the latter can be achieved. The same resonant behavior is maintained regardless of whether the resonator is flow-excited or acoustically excited. Thus, it is suggested that pressure perturbations propagate perpendicularly and acoustically within the resonator throat and cavity. The amplification observed in the vicinity of the resonator displays features typical of TS-wave scattering; however, it is confirmed that this is not solely the result of mean flow distortion due to the geometry and recirculation region. Instead, the results indicate that the phenomenology is a consequence of the combination of scattering, localized non-modal growth, and wall-forcing in the wall-normal direction due to resonance.

I. INTRODUCTION

It is well established that the process of laminar-to-turbulent transition of two-dimensional boundary layers in low-amplitude disturbance conditions is typically governed by linear growth[1] followed by non-linear breakdown[2] of Tollmien–Schlichting (TS) waves.[3] Suppression or delay of TS-wave growth has been the point of focus of numerous past studies in an effort to postpone skin friction increase and, in extent, to increase aerodynamic efficiency in numerous applications.

A plethora of literature is available describing both active and passive approaches for TS-wave suppression, and the examples provided here are by no means exhaustive. Active methods typically rely on the introduction of an opposing perturbation[4] at the vicinity of the wall with devices such as vibrating ribbons[5] and plasma actuators[6] using microphones as feedback sensors. Based on this hardware configuration, filter-based[7,8] and model-based[9,10] closed-loop control schemes have been developed to establish the appropriate perturbation phase with respect to the incoming TS-wave. On the other hand, passive approaches have relied on the development of interfaces between the boundary layer and the wall, which are typically characterized by low surface stiffness. The coupled fluid–structure interaction results in the motion of the interface as a response to flow perturbations that, in turn, attenuates boundary layer perturbations. The interfaces can be continuous such as compliant surfaces,[11,12] where impedance matching between the fluid and the wall is sought for, as well as discrete such as phononic sub-surfaces[13,14] with band-stopping capabilities.

The aforementioned passive devices have a frequency-dependent response to the perturbations of the boundary layer, exhibiting resonant or anti-resonant behaviors. Another family of devices with resonant attributes are the well-known Helmholtz resonators, often modeled in analogy to a mass–spring system.[15] They comprise a rigid enclosure and an open throat, the dimensions of which together define the natural frequency. Various configurations such as shallow cavities and gap flows have been investigated that are of particular interest in the discipline of aeroacoustics due to the relevance of acoustic noise emission and absorption in jet engine liners.[16,17]

When a Helmholtz resonator is excited by a boundary layer, grazing flow conditions are observed. Separation occurs at the most upstream edge of the resonator throat, and the resulting shear layer causes amplification of a Kelvin–Helmholtz (KH) instability that impinges on the most downstream edge of the orifice.[18] The acoustic waves that are generated as a consequence propagate upstream and excite the separated shear layer through its receptivity, thus creating a feedback loop. The feedback can be classified as fluid-dynamic or fluid-resonant.[19] In the fluid-dynamic case, the orifice and acoustic wavelength scales are comparable. The acoustic waves propagate parallel to the shear layer and, hence, directly govern the KH instability causing self-sustained oscillations known as the “Rossiter mode.”[18] In the case of fluid-resonant feedback, the resonator response disturbances instead propagate perpendicularly to the orifice and resonance occurs when the characteristic frequency of the hydrodynamic flow disturbances matches the natural frequency of the cavity.[20,21] Hydrodynamic and acoustic disturbance components are typically separated by momentum potential theory,[22] identifying the cavity dynamics as the primary source of noise generation, specifically separation at the downstream corner of the cavity throat.[23]

In most applications, practical sizes of Helmholtz resonators are sought for, with cavity diameters typically less than a centimeter and even smaller orifice diameters. The natural frequency and orifice diameter of such resonators match well with turbulent boundary layer inner time scales and length scales, respectively. Specifically for shallow cavities, a strong dependence of the flow dynamics to the depth-to-diameter ratio has been observed in various studies,[24,25] leading to either steady, switching, or flapping dynamics. It is important to note that the available literature on grazing flow over resonators and shallow cavities such as in the examples given above primarily focuses on turbulent boundary layers.[26] The premise of this work is, thus, to investigate the salient interactions of a Helmholtz resonator with TS-wave instabilities in laminar boundary layers, aiming to assess its suitability for passive flow control.

To the best of authors’ knowledge, there is currently very limited availability of studies directly treating the coupling/feedback effects of Helmholtz resonators and TS-waves, although early as well as later investigations with streamwise extending resonator arrays and perforated walls have shown destabilizing effects.[27,28] The majority of the available literature focuses on the acoustic absorption and drag increase in sub-surface resonators in the context of acoustic liners in laminar boundary layers grazing over orifices.[29,30] The associated local shear flow dynamics are explored either numerically or experimentally and, commonly, the cavities as well as the full liner walls are modeled based on wall acoustic impedance.[31–33]

Hereby, it must be noted that subjecting a Helmholtz resonator to a laminar boundary layer suggests that interactions interfere with the transition process for which roughness is known to play a critical role. Through the process of receptivity, acoustic or hydrodynamic external disturbances interact with the mean flow distortion caused by roughness elements.[34,35] If the roughness is larger than a certain critical height, instability modes arise and transition occurs at a more upstream location. Substantial research has been performed over the past years regarding the influence on TS-waves of distributed[36] and isolated roughness,[37] either two- or three-dimensional,[38,39] with destabilizing[40,41] as well as stabilizing[42,43] effects being reported. A two-dimensional resonator throat (slit type) can be geometrically considered as an abrupt two-dimensional roughness. For these specific cases, interactions can be modeled by triple-deck theory,[44] indicating that the main mechanism influencing transition is TS-wave scattering caused by roughness-induced mean flow distortion.[45,46]

In this work, a Helmholtz resonator is excited by linearly amplified TS-waves within the unstable region. The resonator is designed such that the orifice is significantly smaller than the characteristic wavelength of the disturbances and as such pertains to fluid-resonant behavior. The aim of the present investigation is twofold. First, the dynamics of the resonator throat are analyzed in order to formulate an equivalent wall impedance, thus determine phase relations between pressure and velocity at the orifice and how they influence the local flow topology. Second, the possibility of stabilization of TS-waves is explored, in relation to mean flow distortion-induced scattering mechanism and how the latter is altered by the dynamics of resonance. To achieve the above, linearized Navier–Stokes (LNS) simulations in conjunction with particle image velocimetry (PIV) and microphone measurements are performed over a zero pressure gradient flat plate where two-dimensional TS-waves are artificially introduced.

II. PROBLEM FORMULATION AND METHODOLOGY

A. General parameters, conventions, and scaling

The analysis of the interaction between the resonator and the boundary layer encompasses results obtained with numerical simulations and wind tunnel experiments at the same conditions. The general parameters of the problem are defined during preliminary studies that involve a marching solution of the laminar boundary layer equations[3] and the solution of the parabolized stability equations[47] (PSE) for incompressible flows. Several experimental considerations are taken into account. To begin with, TS-waves must have amplified to a measurable amplitude and wavelength, without saturation of linear modes or transition to turbulence within the region of interest. At the same time, the frequency of the amplified TS-waves should be sufficiently high, allowing for a reasonably sized resonator that is characterized by a resonance frequency similar to the TS-wave frequency.

Considering the above requirements, the following parameters are defined [refer to Figs. 1 and 2]. The flat plate is 1 m long and is subjected to a freestream velocity of $U_\infty = 20.9\,\mathrm{m/s}$. TS-waves are generated at a distance of 0.18 m from the leading edge for both numerical and experimental approaches. A Cartesian coordinate

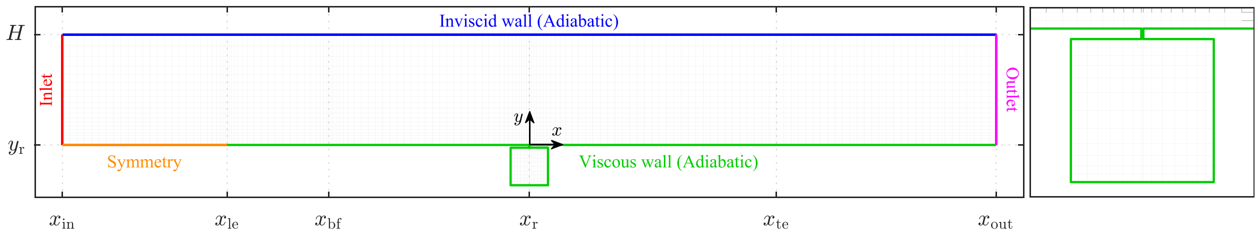

FIG. 1. Overview of the computational domain, mesh, and boundary conditions. Critical streamwise locations are noted representing: the inlet ($x_{in} = -0.85\,\mathrm{m}$), the plate leading edge ($x_{le} = -0.55\,\mathrm{m}$), the body force input ($x_{bf} = -0.37\,\mathrm{m}$), the plate trailing edge ($x_{te} = 0.45\,\mathrm{m}$), and the outlet ($x_{out} = 0.85\,\mathrm{m}$). For visualization purposes, the mesh density has been reduced by 100 times, maintaining the relative element size.

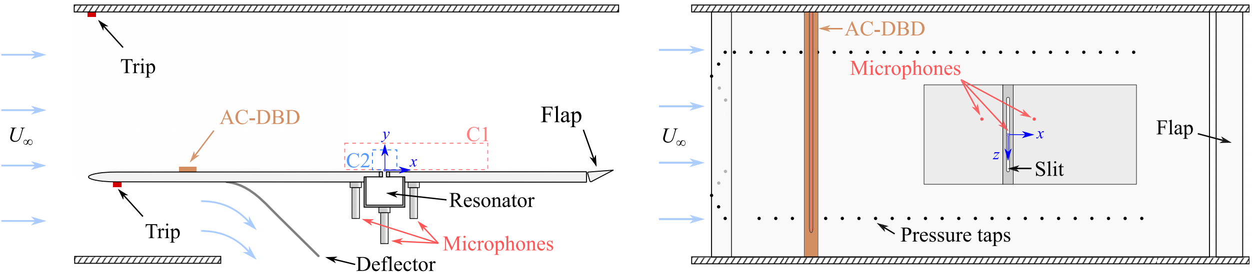

FIG. 2. Side and top overview of the experimental setup. TS-waves are generated with an AC-DBD plasma actuator. A deflector shields the microphones from the incoming flow. PIV measurement fields of view are marked by dashed boxes (not to scale).

system is defined such that $x = 0$ coincides with the center of the resonator throat, 0.18 m from the leading edge, $y = 0$ at the wall surface, and $z = 0$ at the midspan of the flat plate. The spanwise-invariant Helmholtz resonator consists of a square cavity of $68 \times 68\ \mathrm{mm}^2$, and a throat of 1 mm wide and 5 mm long, resulting in an acoustic resonant frequency of approximately 295 Hz (refer to Sec. III B).

Throughout this report, dimensional quantities are noted by their symbol and accompanied by the respective unit (e.g., $x = 1$ mm). For non-dimensional representation, measured and computed quantities are normalized with scaling parameters from the baseline boundary layer and are noted by their symbol without units (e.g., $x = 1$). More specifically, lengths are normalized with the displacement thickness of the baseline boundary layer, $\delta_r^* = 1.1 \times 10^{-3}$ m, at the resonator location, $x = 0$. In turn, frequencies are scaled with the resonator natural frequency, $f_r = 295$ Hz, while velocities with the freestream velocity, $U_\infty = 20.9\ \mathrm{m/s}$. Time-averaged quantities are identified with an overbar (e.g., $\bar{u}$), while fluctuating components are marked by a dash (e.g., u'). Finally, quantities averaged over phase-locked PIV measurements are denoted with chevron brackets (e.g., $\langle u \rangle$).

B. Numerical setup

1. Governing equations, domain, and boundary conditions

The perturbations related to the convection of the TS-waves are of very low amplitude; hence, no three-dimensional effects or saturation of linear modes is expected throughout the domain, including the resonator region. Consequently, simulations may be carried out in a two-dimensional fashion (COMSOL 5.6). At the same time, the assumption of small perturbations implies that it is not necessary to solve for the full Navier–Stokes problem. Instead, the solution entails the linearization of the compressible, non-isothermal Navier–Stokes equations (LNS); hence, a first-order perturbation problem is defined, with respect to a stationary background flow field. The latter is computed via a steady-state solution of the compressible Navier–Stokes equations (NS). In either problem, density is related to pressure and temperature by means of the ideal gas equation of state. For the purpose of this work, the LNS problem is solved in the frequency domain.

An overview of the computational domain along with the boundary conditions and the mesh is shown in Fig. 1. The primary region of interest is 1 m long, extending from the leading edge (x_{le}) to the trailing edge (x_{te}) of the flat plate. Within these coordinates as well as around the resonator throat and cavity, an adiabatic viscous wall boundary condition is applied. The wall is extended all the way to the outlet (x_{out}) in order to ensure that any outlet boundary condition effects are not affecting the field at x_{le}. In order to reduce computational costs, an adiabatic inviscid wall condition is applied at the top boundary as it is not necessary to resolve the local boundary layer. The domain height (H) is set to 0.2 m, approximately 140 times higher than the unperturbed boundary layer displacement thickness at x_{te}, minimizing the influence of the upper boundary condition on the TS-waves. From the inlet up to the leading edge, a symmetry condition is applied, mitigating downstream propagation of leading-edge pressure gradient effects.[48]

The aforementioned wall and symmetry boundary conditions are kept the same regardless whether solving for the steady-state field (NS) of the perturbation field (LNS). Instead, the inlet and outlet boundary conditions are adjusted accordingly. Hence, for the NS problem, the inlet boundary condition is a constant normal velocity ($U_\infty = 20.9\ \mathrm{m/s}$) and isothermal ($T_\infty = 20\,^\circ\mathrm{C}$). At the same time, at the outlet, a zero relative static pressure condition and heat flux are applied, ensuring convective heat transfer through the outlet. On the other hand, for the LNS problem the inlet and outlet boundaries are extended to include absorbing layer domains (perfectly matched layers), where acoustic and convective wave perturbations are exponentially attenuated by means of complex coordinate stretching.[49,50]

2. Numerical Tollmien–Schlichting wave generation

Disturbances are introduced by means of an unsteady body force source (F_{bf}) located at x_{bf} and acting along the x direction. The source is applied over a rectangular domain ($4 \times 0.5\ \mathrm{mm}^2$), at a distance of 0.1 mm from the wall. In order to ensure smooth transition to the body force domain, the source is given a two-dimensional cosine distribution

$$F_{\mathrm{bf}} = \frac{A_{\mathrm{bf}}}{2} \times \left[1 - \cos\left(\frac{2\pi}{l_{\mathrm{bf}}} x\right)\right] \times \left[1 - \cos\left(\frac{2\pi}{h_{\mathrm{bf}}} y\right)\right], \qquad (1)$$

where l_{bf} and h_{bf} are the width and height of the body force domain, respectively. In turn, A_{bf} corresponds to a sinusoidal unsteady disturbance at the desired frequency, whose amplitude is selected such that the reference TS-wave amplitude at the resonator location matches the experimental measurements. The range of TS-wave frequencies hereby investigated lies between 200 and 400 Hz. When determining the background steady-state field, A_{bf} is set to zero.

3. Spatial discretization

The NS and LNS problems are discretized in space with second-order Lagrangian finite elements on a structured mesh as seen in Fig. 1. At critical locations where strong velocity and pressure gradients are expected $(x_{\mathrm{le}}, x_{\mathrm{bf}}, x_{\mathrm{r}})$, mesh density is increased to maintain accuracy. The aspect ratio of the elements in the aforementioned regions and within the resonator throat is 1:1. From thereon, the element size is gradually increased at a rate of 10% to reach aspect ratios of 3.5:1 and 1:10 along the streamwise and wall-normal directions, respectively.

The minimum element size is determined by considering the viscous and thermal boundary layer thicknesses in the resonator throat that need to be resolved. Under the assumption that within the throat and the cavity the phenomena are primarily acoustic, these thicknesses can be estimated as the acoustic viscous and thermal penetration depths,[51] expressed as $\delta_\mu = \sqrt{2\mu_\infty/\omega\rho_\infty}$ and $\delta_\kappa = \delta_\mu/\sqrt{\mathrm{Pr}}$, respectively, where μ_∞ and ρ_∞ are the freestream dynamic viscosity and density, ω is the angular frequency of the wave, and Pr is the freestream Prandtl number. Hereby, $\delta_\mu < \delta_\kappa$; hence, the minimum element size is set to $\epsilon_{\min} = \delta_\mu$, resolving up to a wave of angular frequency of $\omega = 2\pi \cdot 400\,\mathrm{rad}$. Considering the second-order Lagrangian spatial discretization, the minimum distance between element nodes is $\delta_\mu/2 = 5.5 \times 10^{-5}\,\mathrm{m}$, approximately 20 times smaller than δ_{r}^*. The suitability of this mesh size has been verified through a preliminary grid convergence study.

C. Experimental apparatus and techniques

1. Wind tunnel model

Experiments are carried out in the Anechoic wind tunnel (A-tunnel) at Delft University of Technology. The test section is a square cross section of $500 \times 500\,\mathrm{mm}^2$, characterized by a turbulence intensity below 0.05% and outlet uniformity within 0.6%, for the entire range of operating velocities.[52]

An overview of the wind tunnel model is shown in Fig. 2. A 20-mm-thick, 500-mm-wide, and 1000-mm-long flat plate is inserted at 30% of the test section height for alleviating wind tunnel corner effects.[53] The flat plate is manufactured from machined aluminum, finished at a surface roughness of approximately 0.05 mm. Its leading edge is a modified superellipse, ensuring minimal radius of curvature gradient between the ellipsoid and the flat part of the plate.[54] Two pressure tap arrays are located symmetrically with respect to the midspan of the flat plate and extending around the leading edge, thus providing information regarding the streamwise pressure gradient as well as the spanwise pressure uniformity. For eliminating unsteady fluctuations due to separation, the boundary layers at the top wall and the lower side of the flat plate are tripped by means of 2-mm-thick zigzag turbulator. A flap is positioned at the trailing edge of the flat plate, allowing for adjustments of the leading edge stagnation point.

The flat plate bares a large opening where inserts can be interchanged. The two-dimensional Helmholtz resonator is integrated by machining three aluminum inserts that fit into the aforementioned opening, as shown in the top view of Fig. 2. The central insert holds a machined slit with dimensions of 1, 5, and 147 mm along the *x*, *y*, and *z* directions, respectively, that serve as the Helmholtz resonator throat. The span is sufficiently long such that the flowfield at the midspan can be considered two-dimensional and, hence, comparable to 2D simulations. The resonator cavity is a removable box inserted directly under the slit, with dimensions of 76, 60, and 170 mm along the *x*, *y*, and *z* directions, respectively. Care is taken to mitigate possible leaks at the component interfaces by means of adhesives and thin aluminum tape. In order to allow for baseline measurements of the boundary layer without the influence of the resonator, the throat insert can be exchanged with a solid insert of the same dimensions.

2. Experimental Tollmien–Schlichting wave generation

Generation of the TS-waves is achieved by means of a spanwise two-dimensional AC-DBD plasma actuator,[6,55] located at 0.18 m from the leading edge. In this configuration, the plasma actuator is composed of a 3-mm-wide and 60-μm-thick copper strip that acts as the high-voltage electrode and a 60-μm-thick Kapton dielectric, while the aluminum plate is grounded, thus completing the actuator circuit. The total thickness is 120 μm, approximately 20% of the local displacement thickness ($\approx$600 μm); thus, the mechanical roughness associated with the actuator can be considered negligible. The electrical nature of the actuator allows great flexibility for controlling the amplitude and frequency of the introduced excitation. Similar to past works,[56] the forcing signal comprises of short pulses, constructed by modulating a sinusoidal carrier signal (4 kHz, 4 k $\mathrm{V_{pp}}$). The duty cycle is selected such that each pulse completes two carrier frequency cycles, a duration of 50 ms. Bursts of pulses are, then, sustained at the desired TS-wave excitation frequencies (240, 270, 290, 310, and 340 Hz), located near the Helmholtz resonance frequency ($\approx$295 Hz, see Sec. III B).

3. Microphone measurements

Three highly sensitive ($-15\,\mathrm{dBm/Pa}$), calibrated, electret condenser microphones (LinearX M53) are used to monitor pressure amplitudes upstream, downstream, and within the resonator cavity as shown in Fig. 2. The upstream and downstream microphones are each located at a distance of 60 mm from the resonator throat center. They are mounted on the flat plate, directly under tap holes of 0.1 mm of diameter, via a threaded connector that seals by means of a rubber o-ring. Care is taken to ensure that the resonant frequency of the cavity formed between the pressure tap and the microphone surface, which are of $\mathcal{O}(\mathrm{kHz})$, does not interfere with the frequencies of interest, which are of $\mathcal{O}(\mathrm{Hz})$. In turn, the resonator cavity microphone is mounted with the same connector on the cavity walls, directly under the resonator throat. In order to prevent interaction of the incoming flow with the microphones and the resonator cavity, a deflector is mounted at the underside of the flat plate and the trailing-edge flap is adjusted accordingly. All microphone measurements mentioned in this report are performed at a sampling rate of 51.2 kHz over a sampling time of 10 s, unless otherwise stated.

4. Two-component velocity field measurements

Two-component velocity field measurements are performed with particle image velocimetry on the *x*–*y* plane over two regions of interest, defined by the dashed rectangles in the side view of Fig. 2. The first configuration (C1) aims at capturing the evolution and growth of the generated TS-waves as they propagate past the Helmholtz resonator location. In turn, the second configuration (C2) focuses on the region above the resonator throat, aiming at quantifying the local interactions between the TS-waves and the resonator. For both configurations, seeding particles with mean droplet diameter of 1 μm are produced by a fog generator and water–glycol solution. A laser sheet of approximately 1 mm thickness is constructed with a dual cavity Nd:YAG laser (200 mJ/pulse) and a set of cylindrical and spherical lenses. A summary of the relevant measurement parameters is provided in Table I.

In C1, the region of interest is imaged by two cameras whose fields of view are stitched to obtain a combined field of view of 120×20 mm^2 along the streamwise and the spanwise directions, respectively. This region of interest spans from 30 mm upstream to 90 mm downstream with respect to the resonator throat. Images are captured either randomly or phase-locked with respect to the TS-waves, by synchronizing the PIV system with the plasma actuator. In the random measurement case, an ensemble of 2000 images is recorded, allowing estimation of statistical quantities at every streamwise location. In turn, in phase-locked measurements, six phase-averaged velocity fields (1000 realizations) over a full TS-wave cycle are obtained, thus yielding greater accuracy on the wave amplitude estimate. Hereby, particle displacement is calculated by employing a multi-pass, cross-correlation algorithm[57] with interrogation window deformation,[58] from an initial window of 48×48 pixels to a final window of 24×24 pixels and 50% overlap. Spurious vectors are discarded by applying the universal outlier detection technique.[59]

In C2, a smaller field of view is sought just above the resonator throat; hence, only one camera is used, imaging an area of 30×25 mm^2 along the streamwise and spanwise direction, respectively. As in C1, phase-locked measurements are performed, obtaining 12 phase-averaged fields over the TS-wave cycle. For these measurements, the goal is to quantify velocity components near the throat region, i.e., in close proximity of walls where the classical, cross-correlation-based PIV uncertainty is high. Instead, images are processed with particle tracking velocimetry (PTV), tracing the path of individual particles between two consecutive frames. The ensemble of the particle tracks over all realizations is converted to a Cartesian grid by an in-house developed algorithm that employs an adaptive multivariate polynomial regression to determine the velocity components at the desired grid locations. In this manner, spatial resolution and uncertainty are a function of the number of realizations, in this case 1000. The resulting vector pitch is 0.07 mm along both x and y axes, corresponding to approximately six pixels on the camera sensor.

TABLE I. Particle image velocimetry parameters.

Parameter	C1	C2
Sensor resolution	2560×2160 pixels^2	
Pixel pitch (μm)	6.5	
PIV processing type	Cross-correlation	Particle tracking
Lens focal length (mm)	105	200
Aperture ($f_\#$)	5.6	5.6
Frame separation (Δt) (μs)	30	15
Magnification factor	0.26	0.55
Field of view area (mm^2)	120×20	30×25
Vectors per field	410×70	426×360
Vector pitch (mm)	0.3	0.07

Estimation of the time-averaged uncertainty is determined through linear error propagation[60] and linear regression analysis[61] for cross-correlation fields and particle tracking fields, respectively. The corresponding maximum uncertainties with respect to the local velocity are $\varepsilon_{\bar{u}} \approx 0.06\%$ and $\varepsilon_{\bar{v}} \approx 3.2\%$ for cross-correlation, and $\varepsilon_{\bar{u}} \approx 0.2\%$ and $\varepsilon_{\bar{v}} \approx 3.6\%$ for particle tracking.

III. BASELINE CONDITIONS

A. Flat plate boundary layer characteristics

The characterization of the unperturbed flat plate boundary layer is performed in the absence of TS-waves and without the Helmholtz resonator. In the simulations, this is achieved by disabling the resonator's throat and cavity domains (Fig. 1) and replacing the top side of the throat with a viscous, adiabatic wall condition. Similarly, for the experimental measurements, the insert of the resonator throat (Fig. 2) is replaced with a solid one.

The pressure coefficient, $C_p = (p - p_\infty)/(p_0 - p_\infty)$, over the flat plate, estimated by solving the steady-state NS and by pressure tap measurements is shown in Fig. 3(a). Two sets of measurements are provided, corresponding to each of the pressure tap arrays present on the wind tunnel model (Fig. 2). It is evident that both arrays provide the same C_p along the flat plate; hence, the experimental boundary layer can be considered sufficiently two-dimensional. Remarkable agreement between the numerical and experimental methodologies is achieved downstream of $x = -400$, where a near-zero pressure

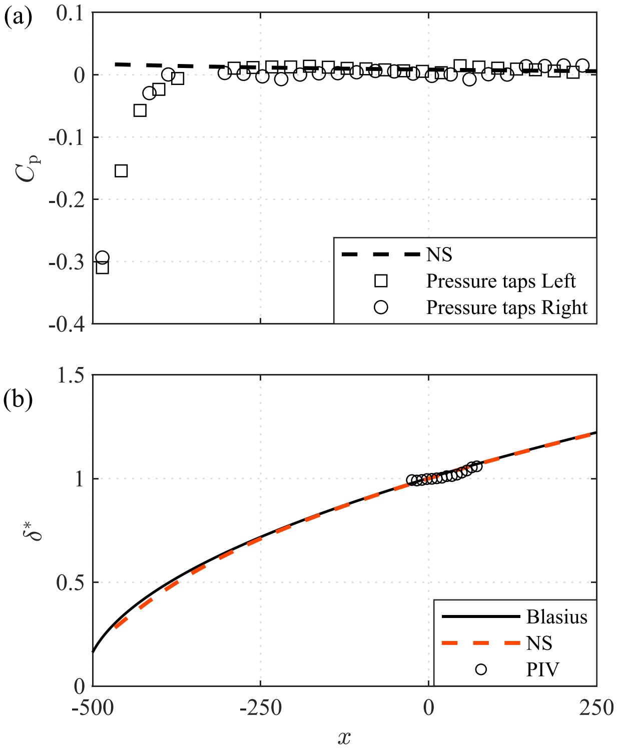

FIG. 3. Comparison of the baseline boundary layer characteristics between simulations and experiments. (a) Pressure coefficient: hereby, marks signify values from the two pressure tap arrays on the model shown in Fig. 2. (b) Displacement thickness: for clarity, the PIV sample points have been reduced by a factor of 60.

gradient is observed. Upstream of $x = -400$, the experimental C_p exhibits a favorable pressure gradient as a consequence of the leading-edge geometry that is not accounted for in the simulations.

Considering the boundary layer itself, the displacement thickness (δ^*) comparison between the Blasius solution, NS simulations, and PIV measurements is shown in Fig. 3(b). Hereby, the PIV measurements correspond to configuration C1 (see Sec. II C 4). As with the C_p, very good agreement between the methodologies is observed, particularly in the vicinity of the resonator region. Small departing between the Blasius solution and the NS simulations is limited in the upstream part of the domain ($x < -250$) and is due to the symmetry boundary condition upstream the leading edge that mitigates leading-edge pressure effects as discussed in Sec. II B 1. Though not shown, similar agreement is identified in the boundary layer momentum thickness and shape factor.

The stability characteristics of the baseline boundary layer are assessed by means of PSE analysis on baseflow velocity fields obtained by both NS simulations and PIV. The PSE equations are marched throughout the domains ($x > -450$ for NS and the full PIV domain) for a range of TS wave frequencies to obtain the corresponding growth rates along the streamwise direction (α_i). The boundary conditions assume zero velocity perturbations ($u' = v' = 0$) at the wall and at the freestream. Figure 4(a) exhibits the estimated neutral stability curve ($\alpha_i = 0$), typical of a Blasius boundary layer, with remarkable agreement between methods in their overlap region. Hereby, the experimentally introduced TS-wave frequencies are also marked, located in the stable region with respect to the neutral stability curve. Five TS-wave frequencies are chosen, the central one being approximately equal to the resonator natural frequency (see Sec. V). Consequently, and in conjunction with the corresponding amplification factors shown in Fig. 4(b), it can be seen that the TS-waves introduced at that frequency range are expected to increase in amplitude as they propagate over the resonator streamwise location ($x = 0$). At the same time, it is important to note that the resonator natural frequency ($f = 1$) lies within the unstable frequency range as observed in the neutral stability curve. Hence, any self-excitation of the resonator can potentially result in the development of TS-waves with frequency equal to the resonator fundamental frequency.

Figure 4(c) shows the vertical velocity fluctuation component (v') of the flowfield for $f = 0.98$, in the vicinity of the resonator throat location. Hereby, the TS-waves can be clearly identified through both LNS and PIV methodologies with substantial agreement. The estimated wavelength range calculated for the experimental and numerical frequency range ($0.68 < f < 1.36$) is $32 < \lambda_{TS} < 17$; i.e., the wavelength decreases for increasing frequency, as predicted from PSE stability analysis. An important aspect is the relative scale difference between the baseline TS-wave wavelength and the resonator throat width, the latter being 0.93. Based on the estimated wavelengths mentioned above, the throat width is at least 18 times smaller than the shortest TS-wave. Consequently, when the resonator is introduced, it is expected that at any moment, the throat will be experiencing a small fraction of the TS-wave pressure front, approximating a two-dimensional input to the resonator. This assumption is central for expressing the frequency response of the resonator (i.e., impedance) as an inhomogeneous boundary condition relating pressure to velocity over the orifice. Confirmation of this assumption is further discussed in Sec. IV B.

B. Resonator acoustic response characteristics

Characterization of the resonator is performed acoustically, i.e., in the absence of flow and the associated convective phenomena, by

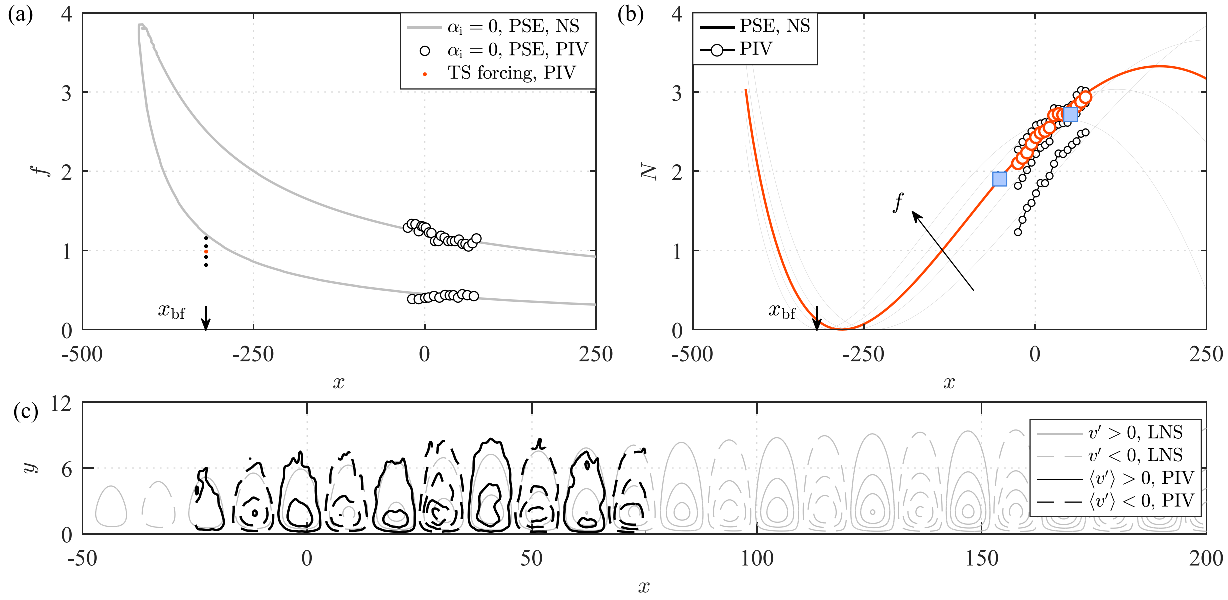

FIG. 4. (a) Neutral stability curve obtained through PSE analysis on the LNS and PIV velocity fields. Dotted marks indicate the streamwise location and frequency of the TS-waves introduced during experiments, with the red mark corresponding to the frequency nearest the resonator resonance ($f = 0.98$). (b) Amplification factor from LNS and PIV for the experimental excitation frequencies. Red data correspond $f = 0.98$, and the arrow indicates the direction of increasing f. The blue squares pertain to microphone measurements for $f = 0.98$. For simulations, $N = \int_{x_0}^{x} -\alpha_i dx$, x_0 being the neutral point. For experiments, $N = \ln(v'/v'_0)$ assuming the same neutral point as in the simulations. (c) Comparison of the vertical velocity fluctuation component of the TS-waves obtained with LNS and phase locked PIV for $f = 0.98$.

appropriately adjusting the numerical and experimental setups. More specifically, for the numerical setup, the problem is solved in the frequency domain formulation of the LNS equations. The resonator is subjected to a planar pressure wave that propagates in the wall normal direction, whose amplitude is 1 Pa, for a range of frequencies. It is noted that due to linearization, the wave perturbation amplitude is unimportant. The computational domain above the resonator is a rectangle of double the size of the resonator and whose boundaries attenuate wave perturbations in the same manner as in the main simulations, i.e., via perfectly matched layers. In turn, for the experimental setup, the freestream velocity is zero, the top wall of the wind tunnel model is removed, and a speaker that produces white noise is placed in the far-field opposite the flat plate. In addition, apart from the resonator cavity microphone, a reference microphone is placed on the surface of the flat plate over the resonator throat. Measurements are performed at a sampling frequency of 27.6 kHz over a sampling time of 30 s.

For both numerical and experimental approaches, a complex frequency response function of the resonator, $H_r(f)$, is obtained by comparing the pressure frequency spectrum at the throat, $p_t(f)$, to the pressure frequency spectrum at the midpoint of the lowest wall of the cavity, $p_c(f)$, i.e., at the physical locations of the microphones. The response function is formulated as

$$H_r(f) = \frac{1}{2}\left[\frac{S_{p_tp_c}(f)}{S_{p_tp_t}(f)} + \frac{S_{p_cp_c}(f)}{S_{p_cp_t}(f)}\right], \tag{2}$$

where $S_{p_tp_t}(f)$ and $S_{p_cp_c}(f)$ are the complex auto-spectra of $p_t(f)$ and $p_c(f)$, respectively ($S_{p_tp_t} = p_t{}^*p_t$ and $S_{p_cp_c} = p_c{}^*p_c$), whereas $S_{p_tp_c}(f)$ and $S_{p_cp_t}(f)$ are the cross-spectra between $p_t(f)$ and $p_c(f)$, using either as a reference ($S_{p_tp_c} = p_t{}^*p_c$ and $S_{p_cp_t} = p_c{}^*p_t$). Note that in the aforementioned expressions, the asterisks signify complex conjugates.

The amplitude and phase response components of H_r are shown in Fig. 5(a), closely matching the typical behavior of a Helmholtz resonator pressure response to acoustic excitation (see, e.g., Ref. 15). The resonant frequency ($f = 1$) is defined as the frequency for which the amplitude response is maximized, corresponding to approximately 295 Hz for the dimensions of the resonator at hand. Evidently, below and above the resonant frequency, p_t and p_c are in phase or out of phase, respectively. It is well established that the resonant frequency shifts when a resonator is excited by a turbulent boundary layer due to turbulent scales being comparable to the orifice size.[62] However, in the current study, the boundary layer is laminar and the TS-wave scales are substantially larger than the orifice; hence, no appreciable shifts in frequency are expected. This is further discussed and confirmed in Sec. IV B.

Given the agreement between experimental and numerical data for H_r, there is confidence in defining a complex inhomogeneous boundary condition, H_{BC}, which expresses the ratio of wall-normal velocity to pressure at the resonator throat, i.e., the local wall impedance

$$H_{BC} = \frac{v_{BC}(f)}{p_{BC}(f)}. \tag{3}$$

The amplitude and phase angle of H_{BC} are shown in Fig. 5(b), closely resembling the behavior of the resonator pressure frequency response, H_r.

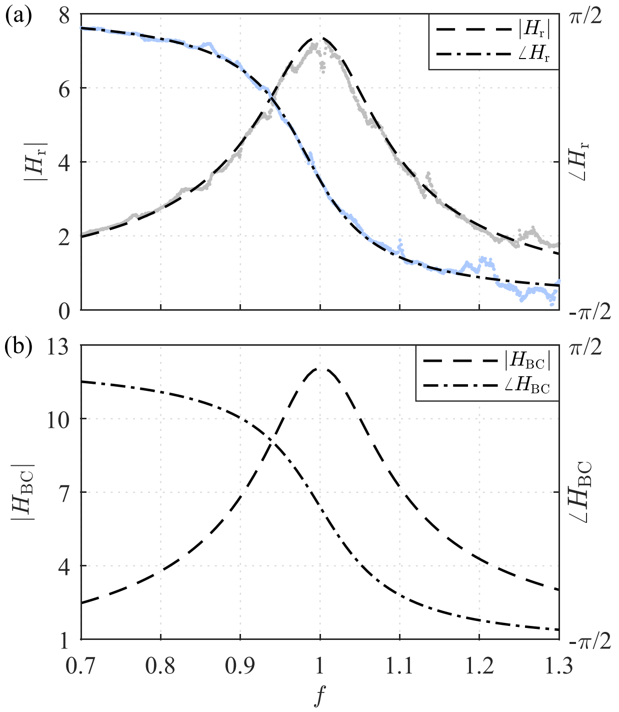

FIG. 5. (a) Complex frequency response function (H_r) of the Helmholtz resonator, determined as the ratio between pressure at the throat ($x = y = 0$) and pressure at the center of the lowest cavity wall. Data points correspond to microphone measurements, whereas lines correspond to simulations. (b) Complex transfer function (H_{BC}) of the wall boundary conditions that model the resonator determined as the ratio between velocity and pressure at the throat ($x = y = 0$).

IV. INTERACTION OF THE HELMHOLTZ RESONATOR WITH THE EXTERNAL FLOW

A. Unperturbed mean flow characteristics

Having characterized the baseline conditions in Sec. III, the mean flow field as a result of the resonator in the absence of TS-waves is investigated. The time-averaged, wall-normal velocity component at the resonator orifice is shown in Fig. 6(a). Similarly to resonators subjected to turbulent boundary layers, separation occurs at the upstream edge of the resonator. The resulting grazing shear layer impinges on the downstream edge of the orifice forming a stagnation point just below $y = 0$, thus being partly deflected toward the throat and forming a recirculation region. No further separation is detected for the current conditions downstream the orifice.

The presence of the orifice is expected to have an influence on the boundary layer integral characteristics. To quantify it, the displacement thickness in the vicinity of the orifice is drawn in Fig. 6(b). Compared to the baseline conditions and according to the steady-state NS solution, the displacement thickness is reduced by less than 0.1% over the orifice. No appreciable change of δ^* is evident in the experimental data.

At the same time, PTV measurements can provide an indication of the extent of interaction of the orifice with the natural perturbations in the boundary layer. The kinetic energy of the measured perturbations near the wall surface ($y = 0.1$) is plotted on Fig. 6(b). A sharp

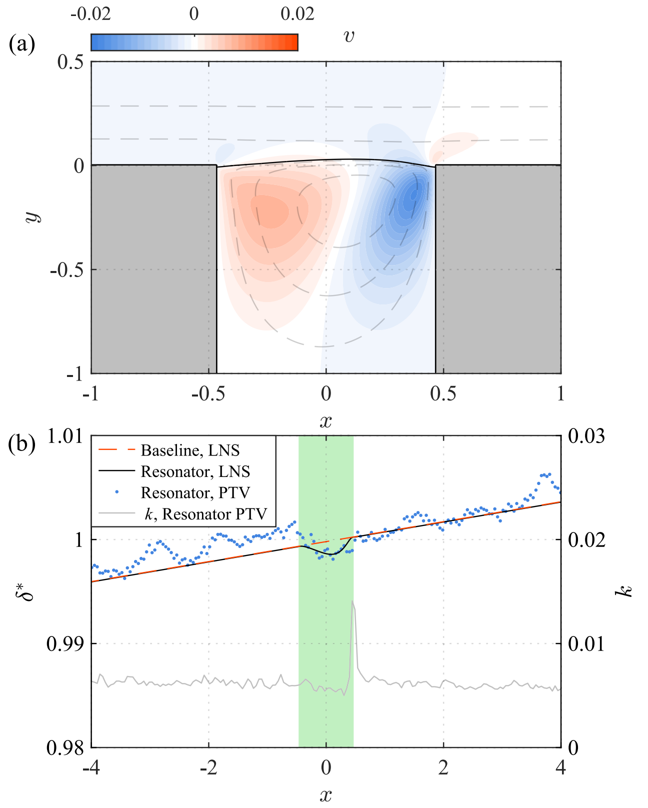

FIG. 6. (a) Vertical velocity component of the steady-state background flow in the vicinity of the resonator throat, determined by the compressible NS equations. Dashed lines depict representative streamfunction levels. The solid black line indicates the dividing streamline (streamfunction of zero). (b) Effect of the resonator throat on δ^* compared to the baseline conditions, as obtained with LNS and PTV. The kinetic energy near the wall ($y = 0.1$) along the streamwise direction obtained with PTV is also provided. The orifice streamwise extent is indicated by the green shaded region.

increase in k is observed at the most downstream edge of the orifice; however, it shortly recedes to the same levels as upstream of the orifice. This behavior is associated with the weak emergence of the Rossiter mode,[18] in this case caused by the small-scale natural turbulence intensity of the tunnel that are of the same length scale as the orifice width. Given the above, and in conjunction with the limited change of δ^*, it is concluded that the presence of the resonator does not influence the baseline boundary layer and, as discussed further in Sec. IV C, its roughness does not contribute in substantial changes in the TS-wave stability.

B. Dynamics of the resonator throat

Local interactions of the body force generated TS-wave with the resonator are assessed by considering the wall-normal perturbation component in the vicinity of the resonator. Figure 7(a) depicts a representative phase of v' in the TS-wave cycle for $f = 0.98$. A direct observation is that due to the large-scale difference between the resonator throat and the TS-wave wavelength (approximately 20 to 1), the area of interaction is limited to the near-wall region of the wave, within δ^*.

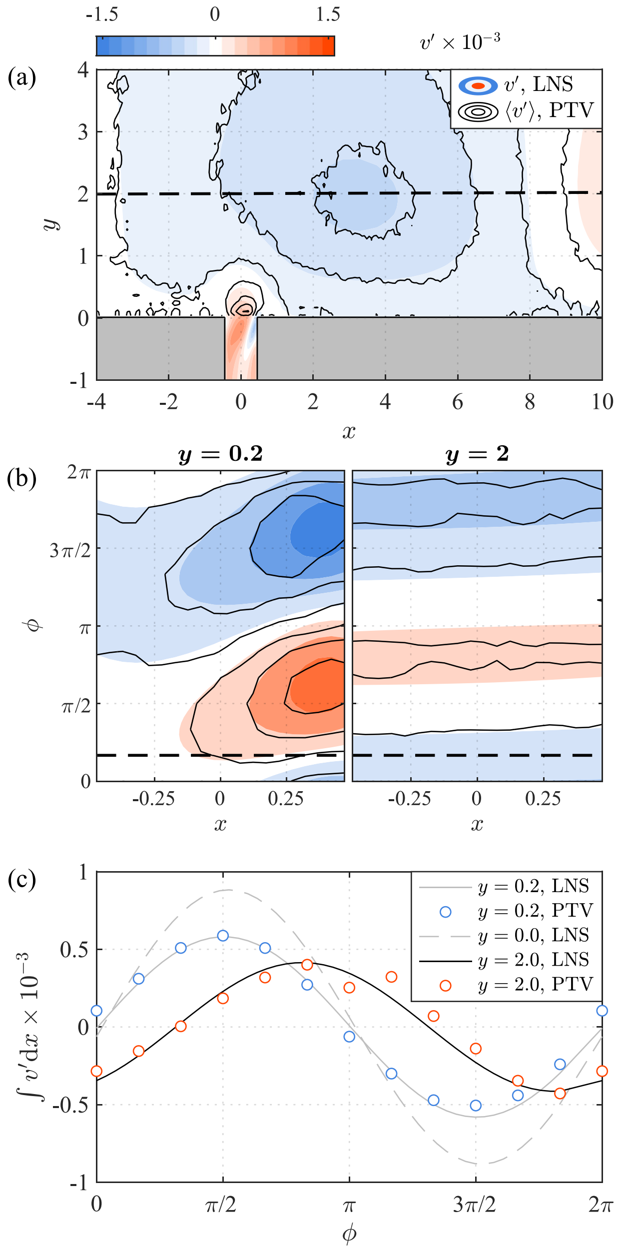

FIG. 7. (a) Comparison of the vertical velocity fluctuation component near the throat obtained with LNS (contour) and phase locked PTV (isolines) at a representative phase ($\phi = \pi/6$) at $f = 0.98$. (b) Distribution of v' along the throat at $y = 0.2$ from LNS (contour) and phase-locked PTV (isolines) over a full TS wave cycle. (c) Integral of v' over the throat over a full TS wave cycle. Dashes indicate $y = 2$ and $\phi = \pi/6$ in (a) and (b), respectively.

Thus, in conjunction with the observations for the unperturbed mean flow, it is concluded that the resonator is not affecting the main body of the TS-wave, located at $y = 2$.

In turn, the relative dynamics between the resonator throat and the main body of the TS-wave are identified by comparing the streamwise distribution of v' over the throat at $y = 0.2$ and $y = 2$, shown in

Fig. 7(b). Unlike v' at $y = 2$, the distribution is not uniform along the streamwise direction near the resonator throat. Instead, the highest amplitudes are skewed toward the downstream direction ($x > 0$), a natural consequence of the grazing boundary layer over the opening. It follows that the wall-normal velocity response of the resonator exhibits a phase lag with respect to the TS-wave, ranging from $\pi/2$ to $\pi/4$ along the throat.

When the integral of v' along the orifice ($y = 0$) is considered as shown in Fig. 7(c), it can be observed that the integrated throat velocity amplitude is approximately twice with respect to the TS-wave ($y = 2$). Given that the data shown pertain to $f = 0.98$, i.e., close to resonance, this corresponds to the maximum wall-normal perturbation amplitude that the investigated resonator configuration can produce. It is of the order of 10^{-3} with respect to the local freestream velocity; hence, local interactions can be considered linear. At the same time, Fig. 7(c) demonstrates that within the TS-wave cycle, there is on average a 0.3π delay between the TS-wave and the orifice wall-normal velocities for the resonance case. For the full range of frequencies tested, from below to above resonance, this delay spans from 0.4π to 0.25π, respectively. Previous works have identified that the optimal phase difference between these velocities for TS-wave cancelation is to be $\pi/2$.[7] Evidently, the physical mechanism that drives the resonator, i.e., a response to the TS-wave pressure fluctuation, cannot produce such a phase difference; hence, a Helmholtz resonator is expected to always amplify TS-waves, as discussed further in Sec. IV C.

In Sec. III B, the frequency response of the resonator has been identified by exciting the resonator acoustically. To establish changes in the resonator frequency response due to TS-wave excitation as well as the presence of the recirculation region, the complex impedance transfer function, H_{BC}, [Eq. (3)] is calculated along the orifice for a range of TS-wave frequencies. The amplitude and phase of H_{BC} at $x = y = 0$ for the two excitation methods are shown in Fig. 8(a). Note that $|H_{\text{BC}}|$ is hereby normalized by its maximum value for comparative reasons. When excited with a TS-wave, the resonance frequency remains virtually unchanged (within 0.5%). However, the corresponding bandwidth is significantly reduced, implying that losses in the throat are higher when the excitation is acoustic.

The complete transfer function over the orifice ($y = 0$) with TS-wave excitation is, in turn, shown in Fig. 8(b). It is observed that the maximum amplitude and zero phase are achieved at different frequencies along the streamwise direction, a direct consequence of the presence of the recirculation region dynamics discussed earlier in this section. Nonetheless, $|H_{\text{BC}}|$ is maximized close to the orifice center (within 8% of the orifice width). Of interest is that the response bandwidth significantly widens toward the trailing edge of the orifice. Combined with the observations regarding the kinetic energy of the unperturbed field shown in Fig. 6(b), the orifice trailing edge is identified as a location of strong interactions between the resonator and the laminar boundary layer, regardless of the excitation frequency.

In contrast to acoustic excitation, $\angle H_{\text{BC}}$ is non-uniform along the orifice. Consequently, TS-waves hold a different average phase between pressure and velocity along x based on their characteristic frequency. More specifically, below, at, and above the resonant frequency, as seen in Fig. 8(b), the average phase relation tends toward π, zero, and $-\pi$, respectively. Nonetheless, this is found to apply only within the recirculation region, below which the phase relations collapse on the acoustic excitation ones. In all, the throat dynamics described infer that pressure perturbations due to the TS-wave at the orifice can be considered to propagate perpendicularly and acoustically within the resonator throat and cavity; thus, modeling the resonator based on its acoustic impedance is an admissible first-order approximation.

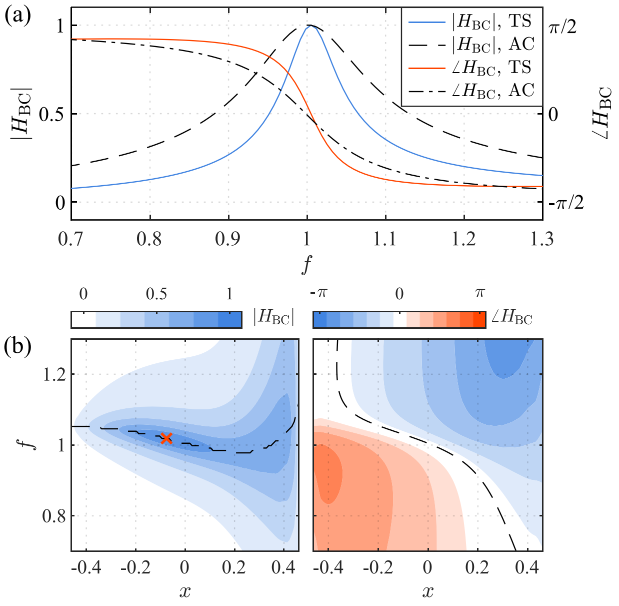

FIG. 8. Complex transfer function (H_{BC}) determined as the ratio between velocity and pressure obtained with LNS. (a) Comparison of H_{BC} between excitation of the resonator acoustically [see Fig. 5(b)] or with the TS-wave ($x = y = 0$). (b) Amplitude and phase of H_{BC} along the orifice ($y = 0$) for excitation with TS-waves. Dashed lines signify maximum amplitude and zero phase along the streamwise direction. The red mark indicates the maximum H_{BC}.

C. Influence of the resonator on TS-wave stability

The influence of the resonator on the stability of the convective TS-waves along the streamwise direction is assessed by considering the amplification factors of the streamwise and wall-normal velocity fluctuation components. The amplification factor formulation[47] with respect to each velocity component is

$$N_{u'} = \ln\frac{|u'|}{|u'|_0}, \qquad N_{v'} = \ln\frac{|v'|}{|v'|_0}, \tag{4}$$

where the reference amplitudes ($|u'|_0, |v'|_0$) are defined from the PSE solution of the baseline case (see Sec. III A). For both numerical and experimental data, streamwise and wall-normal fluctuation amplitudes are extracted at $y = 0.6\delta^*$ and $y = 2\delta^*$, i.e., where they are maximized. With regard to the experimental data, it must be noted that fluctuation amplitudes are defined as the standard deviations of u and v.

Figure 9 compares the aforementioned amplification factors for the baseline and resonator cases pertaining to $f = 0.95$. A few key observations can be made. To begin with, there is a remarkable agreement in both $N_{u'}$ and $N_{v'}$ between the LNS and PIV datasets, particularly in the vicinity of the resonator orifice. This agreement persists downstream of the orifice and, consequently, all the interactions taking place between the resonator and the TS-wave can be considered linear,

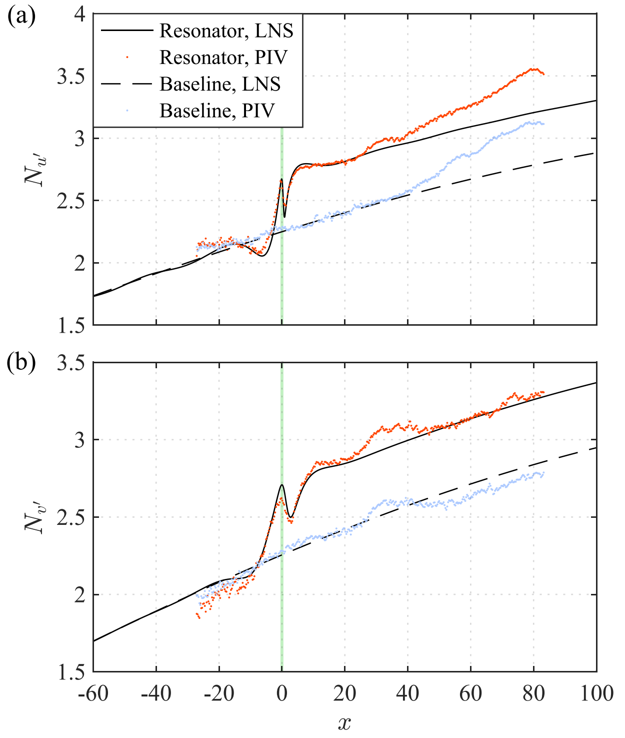

FIG. 9. Amplification factors based on (a) u' and (b) v' for $f = 0.95$ determined from LNS and PIV. The green shaded region indicates the orifice streamwise extent.

confirming initial assumptions. A departure of the PIV from the LNS estimations with increase in $N_{u'}$ is evident downstream of $x = 40$; however, this is not the case for $N_{v'}$. This behavior is independent of the resonator interactions as it is also apparent in the baseline case in the absence of a resonator; hence, it is attested to the emergence of non-linear effects in the baseline experimental boundary layer.

A second observation is that the region of influence of the resonator on the TS-wave extends substantially toward both upstream and downstream directions $(-20 \leq x \leq 20)$. After the interaction with the resonator orifice, the TS-wave proceeds to grow at the same rate as it would in the baseline case, albeit at a higher amplitude; hence, the interaction can be considered local rather than global. This occurs for frequencies below and above resonance as shown in the data in blue on Fig. 10. Of interest is the fact that at the most upstream location where interaction becomes evident, a decrease in amplification factor with respect to the baseline case is observed for both velocity components. It is noted that the resulting amplification factors do not follow a resonant behavior (i.e., increase and decrease while crossing resonance) but is rather reduced as the frequency increases. This is a direct consequence of the phase relation between the TS-wave and the resonator, i.e., as the frequency decreases wall-normal velocity components of the TS-wave and the resonator throat are closer to being in-phase, thus promoting TS-wave growth. Although these considerations may explain the general trend of amplification far upstream and far downstream of the orifice, they do not suffice in describing the phenomenology in the vicinity of the throat, suggesting that multiple effects are in play.

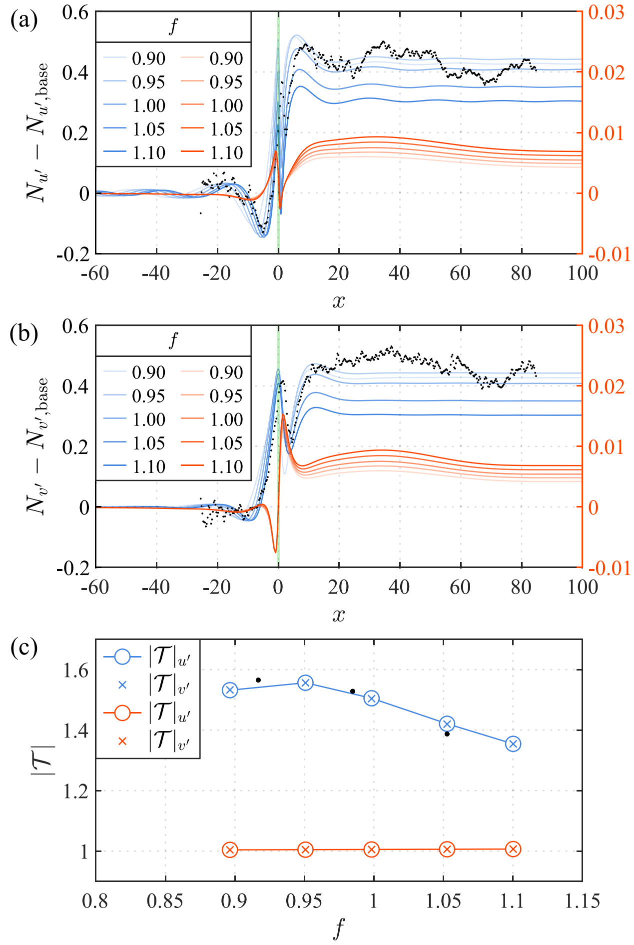

FIG. 10. Difference of amplification factors based on (a) u' and (b) v' with respect to the baseline conditions for different TS-wave frequencies as determined with LNS. The green shaded region indicates the orifice streamwise extent, and points correspond to PIV data for $f = 0.95$. (c) Transmission coefficient[46] based on u' and v', points representing PIV data. Data and axes in red pertain to simulations with the throat only, replacing the resonating cavity with a rigid wall.

The behavior of consecutive reduction-increase-reduction-increase in amplification factor seen in Figs. 9 and 10 is a typical feature of local scattering at isolated small-scale roughness elements and is associated with localized mean flow distortion.[46] To assess the impact of the mean flow distortion caused by the throat geometry on the TS-wave stability, ancillary LNS simulations are performed where the resonant cavity is replaced by a rigid wall while maintaining the full throat geometry. The resulting amplification factors with respect to the baseline case are shown in red in Fig. 10. Scattering behavior is observed for all TS-wave frequencies in the vicinity of the orifice with the amplification factors increasing for increasing frequency, a direct effect of the decreasing wavelength of the TS-waves that causes larger part of the wave to interact with the orifice. Nonetheless, the increase in amplification factor is an order of magnitude less than with the presence of the resonating cavity; thus, the mean flow distortion due to the localized roughness has limited impact on the observed

TS-wave growth. The same conclusion can be drawn by formulating the N factor increment as a transmission coefficient[45] ($\Delta N = \ln \mathcal{T}$) as shown in Fig. 10(c). In the absence of the resonating cavity, $|\mathcal{T}| \approx 1$, thus the impact of the orifice on stability is negligible. In contrast, for the full resonator, $|\mathcal{T}| > 1$, signifying substantial destabilization. Finally, it must be stressed that although similar, the amplification factors based on u' and v' do not match over the orifice (Figs. 9 and 10). This suggests the manifestation of non-modal growth[63] that is localized in the throat vicinity.

Combining the above, it is possible to bring forward the conjecture that the observed amplification phenomenology is a consequence of three distinct effects: localized non-modal amplification over the orifice, wall-forcing in the wall-normal direction caused by the dynamic response of the resonator, and scattering. It is suggested that the wall-normal forcing and non-modal growth act as modifiers of the effective wall distortion that the TS-wave perceives at each phase, affecting scattering properties. The variation of this effective deformation is directly connected to the strict phase relation of pressure and velocity within the TS-wave as well as the characteristic amplitude and phase response of the resonator to external perturbations.

V. CONCLUDING REMARKS

The salient features of the interaction between a two-dimensional Helmholtz resonator with TS-waves are investigated experimentally and numerically for a range of frequencies from below to above resonance. The resonator orifice width is approximately 20 times smaller than the characteristic wavelength of the TS-waves, for which a remarkable agreement between PIV measurements and LNS simulations is achieved. Due to this agreement between measurements and a linear model, it is deduced that the observed phenomenology is governed by linear interactions.

Time-averaged and steady-state results exhibit the typical recirculation region within the resonator throat. In addition, they indicate that interactions are limited to the near-wall region and, more specifically, toward the trailing edge of the resonator orifice noting, however, that the influence of the orifice on the displacement thickness and turbulent kinetic energy of the boundary layer is minimal.

The integral of wall-normal velocity fluctuation along the orifice ($y = 0$) is found to have a fixed phase difference with respect to that of the main body of the TS-wave. This phase difference ranges from 0.4π to 0.25π for increasing frequency and increasingly diverts from the optimal $\pi/2$ necessary for TS-wave attenuation. Thus, it is concluded that a single degree of freedom Helmholtz resonator can only result in amplification and not stabilization of TS-waves.

The frequency response function (i.e., impedance) formulated along the orifice stipulates that there is no substantial shift of resonant frequency when the resonator is subjected to TS-wave excitation rather than acoustic planar waves. At the same time, below the recirculation region, all phase relations collapse to the acoustic excitation case, implying that perturbations can be considered to propagate acoustically within the resonator throat and cavity. Hence, given the scale difference between the wavelength of TS-waves and the orifice, it is suggested that the acoustic impedance is an admissible first-order approximation for modeling the resonator as an inhomogeneous boundary condition.

When considering the amplification factor, the interaction of the resonator is found to be local rather than global; i.e., amplification only takes place in the vicinity of the resonator. The interaction exhibits features typical of scattering; hence, it extends in both upstream and downstream directions. Ancillary simulations without the resonating cavity but with the full throat geometry and recirculation confirm that scattering due mean flow distortion has little impact on the stability of the TS-waves. It is suggested that the observed amplification is a consequence of forcing in the wall-normal direction due to the resonator dynamics and non-modal growth over the orifice, which together cause an apparent mean flow deformation that the TS-wave perceives at each phase, accentuating the scattering behavior.

ACKNOWLEDGMENTS

This research has been supported by the Dutch Research Council (NWO) under the Open Competition Domain Science M funding scheme (Grant No. OCENW.M20.186).

AUTHOR DECLARATIONS

Conflict of Interest

The authors have no conflicts to disclose.

Author Contributions

Theodoros Michelis: Formal analysis (equal); Methodology (equal); Validation (equal); Writing – original draft (equal); Writing – review & editing (equal). **Coert de Koning:** Formal analysis (equal); Methodology (equal); Validation (equal); Writing – original draft (equal); Writing – review & editing (equal). **Marios Kotsonis:** Formal analysis (equal); Methodology (equal); Validation (equal); Writing – original draft (equal); Writing – review & editing (equal).

DATA AVAILABILITY

The data that support the findings of this study are available from the corresponding author upon reasonable request.

REFERENCES

[1] H. L. Reed, W. S. Saric, and D. Arnal, "Linear stability theory applied to boundary layers," Annu. Rev. Fluid Mech. **28**, 389–428 (1996).

[2] Y. S. Kachanov, "Physical mechanisms of laminar-boundary-layer transition," Annu. Rev. Fluid Mech. **26**, 411–482 (1994).

[3] H. Schlichting and K. Gersten, *Boundary-Layer Theory*, 9th ed. (Springer, Berlin, Heidelberg, 2017).

[4] A. S. W. Thomas, "The control of boundary-layer transition using a wave-superposition principle," J. Fluid Mech. **137**, 233–250 (1983).

[5] H. W. Liepmann, G. L. Brown, and D. M. Nosenchuck, "Control of laminar-instability waves using a new technique," J. Fluid Mech. **118**, 187–200 (1982).

[6] M. Kotsonis, "Diagnostics for characterisation of plasma actuators," Meas. Sci. Technol. **26**, 092001 (2015).

[7] M. Kotsonis, R. K. Shukla, and S. Pröbsting, "Control of natural Tollmien–Schlichting waves using dielectric barrier discharge plasma actuators," Int. J. Flow Control **7**, 37–54 (2015).

[8] B. Simon, N. Fabianne, T. Nemitz, S. Bagheri, D. S. Henningson, and S. Grundmann, "In-flight active wave cancelation with delayed-x-LMS control algorithm in a laminar boundary layer," Exp. Fluids **57**, 160 (2016).

[9] B. A. Belson, O. Semeraro, C. W. Rowley, and D. S. Henningson, "Feedback control of instabilities in the two-dimensional Blasius boundary layer: The role of sensors and actuators," Phys. Fluids **25**, 054106 (2013).

[10] H. J. Tol, C. C. de Visser, and M. Kotsonis, "Experimental model-based estimation and control of natural Tollmien–Schlichting waves," AIAA J. **57**, 2344–2355 (2019).

[11] P. W. Carpenter and A. D. Garrad, "The hydrodynamic stability of flow over Kramer-type compliant surfaces. I. Tollmien–Schlichting instabilities," J. Fluid Mech. **155**, 465–510 (1985).

[12] C. Davies and P. W. Carpenter, "Numerical simulation of the evolution of Tollmien–Schlichting waves over finite compliant panels," J. Fluid Mech. **335**, 361–392 (1997).

[13] M. I. Hussein, S. Biringen, O. R. Bilal, and A. Kucala, "Flow stabilization by subsurface phonons," Proc. R. Soc. A **471**, 20140928 (2015).

[14] C. J. Barnes, C. L. Willey, K. Rosenberg, A. Medina, and A. T. Juhl, "Initial computational investigation toward passive transition delay using a phononic subsurface," AIAA Paper No. 2021–1454, 2021.

[15] R. Ma, P. E. Slaboch, and S. C. Morris, "Fluid mechanics of the flow-excited Helmholtz resonator," J. Fluid Mech. **623**, 1–26 (2009).

[16] X. Dai and Y. Aurégan, "A cavity-by-cavity description of the aeroacoustic instability over a liner with a grazing flow," J. Fluid Mech. **852**, 126–145 (2018).

[17] L. Rego, F. Avallone, D. Ragni, D. Casalino, and D. Hervé, "Acoustic liners for jet-installation noise reduction," J. Sound Vib. **537**, 117189 (2022).

[18] J. E. Rossiter, "Wind tunnel experiments on the flow over rectangular cavities at subsonic and transonic speeds," Technical Report No. 64037 (RAE, 1964).

[19] D. Rockwell and E. Naudascher, "Self–sustained oscillations of impinging free shear layers," Annu. Rev. Fluid Mech. **11**, 67–94 (1979).

[20] M. Inagaki, O. Murata, T. Kondoh, and K. Abe, "Numerical prediction of fluid-resonant oscillation at low Mach number," AIAA J. **40**, 1823–1829 (2002).

[21] S. Mallick, R. Shock, and V. Yakhot, "Numerical simulation of the excitation of a Helmholtz resonator by a grazing flow," J. Acoust. Soc. Am. **114**, 1833 (2003).

[22] P. E. Doak, "Momentum potential theory of energy flux carried by momentum fluctuations," J. Sound Vib. **131**, 67 (1989).

[23] Y. W. Ho and J. W. Kim, "A wall-resolved large-eddy simulation of deep cavity flow in acoustic resonance," J. Fluid Mech. **917**, A17 (2021).

[24] M. Hidawa, T. Kawamura, I. Mabuchi, and M. Kumada, "Some characteristics of flow pattern and heat transfer past a circular cylindrical cavity," Bull. JSME **26**, 1744–1752 (1983).

[25] P. W. McCarthy and A. Ekmekci, "Flow features of shallow cylindrical cavities subject to grazing flow," Phys. Fluids **34**, 027115 (2022).

[26] F. Ghanadi, N. Arjomandi, B. Cazzolato, and A. Zander, "Interaction of a flow-excited Helmholtz resonator with a grazing boundary layer," Exp. Therm. Fluid Sci. **58**, 80 (2014).

[27] P. B. Rhines and E. L. Mollo-Christensen, "Boundary layer oscillations over a resonant surface," Phys. Fluids **10**, 916–926 (1967).

[28] A. Rouviere, F. Méry, J. Methel, O. Vermeersch, and M. Forte, "Experimental and numerical study on wall impedance effects on Tollmien–Schlichting Waves," AIAA J. **60**, 508–519 (2022).

[29] G. Kooijman, A. Hirschberg, and J. Golliard, "Acoustical response of orifices under grazing flow: Effect of boundary layer profile and edge geometry," J. Sound Vib. **315**, 849–874 (2008).

[30] Q. Zhang and D. J. Bodony, "Numerical investigation of a honeycomb liner grazed by laminar and turbulent boundary layers," J. Fluid Mech. **792**, 936–980 (2016).

[31] M. Taktak, "An indirect method for the characterization of locally reacting liners," J. Acoust. Soc. Am. **127**, 3548–3559 (2010).

[32] L. Enghardt and A. Fischer, "Determination of the impedance for lined ducts with grazing flow," AIAA Paper No. 2012-2243, 2012.

[33] D. K. Singh and S. W. Rienstra, "Nonlinear asymptotic impedance model for a Helmholtz resonator liner," J. Sound Vib. **333**, 3536–3549 (2014).

[34] W. S. Saric, H. L. Reed, and E. J. Kerschen, "Boundary-layer receptivity to free-stream disturbances," Annu. Rev. Fluid Mech. **34**, 291–319 (2002).

[35] A. V. Fedorov, "Transition and stability of high-speed boundary layers," Annu. Rev. Fluid Mech. **43**, 79–95 (2011).

[36] T. C. Corke, A. Barsever, and M. V. Morkovin, "Experiments on transition enhancement by distributed roughness," Phys. Fluids **29**, 3199–3213 (1986).

[37] M. Asai, M. Minagawa, and M. Nishioka, "The instability and breakdown of a near-wall low-speed streak," J. Fluid Mech. **455**, 289–314 (2002).

[38] Y.-S. Wie and M. R. Malik, "Effect of surface waviness on boundary-layer transition in two-dimensional flows," Comput. Fluids **27**, 157–181 (1998).

[39] M. D. Ma'mun, M. Asai, and A. Inasawa, "Effects of surface corrugation on the stability of a zero-pressure-gradient boundary layer," J. Fluid Mech. **741**, 228–251 (2014).

[40] M. Lessen and S. T. Gangwani, "Effect of small amplitude wall waviness upon the stability of the laminar boundary layer," Phys. Fluids **19**, 510–513 (1976).

[41] J. M. Floryan and M. Asai, "On the transition between distributed and isolated surface roughness and its effect on the stability of channel flow," Phys. Fluids **23**, 104101 (2011).

[42] C. Cossu and L. Brandt, "Stabilization of Tollmien–Schlichting waves by finite amplitude streaks in the Blasius boundary layer," Phys. Fluids **14**, L57–L60 (2002).

[43] J. H. M. Fransson, L. Brandt, A. Talamelli, and C. Cossu, "Experimental study of the stabilization of Tollmien–Schlichting waves by finite amplitude streaks," Phys. Fluids **17**, 054110 (2005).

[44] H. Xu, S. J. Sherwin, P. Hall, and X. Wu, "The behaviour of Tollmien–Schlichting waves undergoing small–scale localised distortions," J. Fluid Mech. **792**, 499–525 (2016).

[45] X. Wu and L. W. Hogg, "Acoustic radiation of Tollmien–Schlichting waves as they undergo rapid distortion," J. Fluid Mech. **550**, 307–347 (2006).

[46] X. Wu and M. Dong, "A local scattering theory for the effects of isolated roughness on boundary-layer instability and transition: Transmission coefficient as an eigenvalue," J. Fluid Mech. **794**, 68–108 (2016).

[47] T. Herbert, "Parabolized stability equations," in *Progress in Transition Modelling* (AGARD, 1994), pp. 4–34.

[48] D. C. Jespersen, T. H. Pulliam, and M. L. Childs, "OVERFLOW, turbulence modeling resource validation results," NAS Technical Report No. NAS-2016-01 (NASA Ames Research Center, 2016).

[49] J.-P. Bérenger, "A perfectly matched layer for the absorption of electromagnetic waves," J. Comput. Phys. **114**, 185–200 (1994).

[50] C. M. Rappaport, "Perfectly matched absorbing boundary conditions based on anisotropic lossy mapping of space," IEEE Microwave Guided Wave Lett. **5**, 90–32 (1995).

[51] M. F. Hamilton, Y. A. Ilinskii, and E. A. Zabolotskaya, "Nonlinear two-dimensional model for thermoacoustic engines," J. Acoust. Soc. Am. **111**, 2076–2086 (2002).

[52] R. Merino-Martínez, A. Rubio Carpio, L. Tércio, L. Pereira, S. van Herk, F. Avallone, M. Ragni, and M. Kotsonis, "Aeroacoustic design and characterization of the 3D-printed, open-jet, anechoic wind tunnel of Delft University of Technology," Appl. Acoust. **170**, 107504 (2020).

[53] W. S. Saric and E. White, "Influence of high-amplitude noise on boundary-layer transition to turbulence," AIAA Paper No. 98-2645, 1998.

[54] N. Lin, H. L. Reed, and W. S. Saric, "Effect of leading-edge geometry on boundary-layer receptivity to freestream sound," in *Instability, Transition, and Turbulence* (Springer, 1992), pp. 421–440.

[55] N. Benard and E. Moreau, "Electrical and mechanical characteristics of surface AC dielectric barrier discharge plasma actuators applied to airflow control," Exp. Fluids **55**, 1846 (2014).

[56] T. Michelis, S. Yarusevych, and M. Kotsonis, "Response of a laminar separation bubble to impulsive forcing," J. Fluid Mech. **820**, 633–666 (2017).

[57] F. Scarano and M. Riethmuller, "Advances in iterative multigrid PIV image processing," Exp. Fluids **29**, S051–S060 (2000).

[58] F. Scarano, "Iterative image deformation methods in PIV," Meas. Sci. Technol. **13**, R1–R19 (2002).

[59] J. Westerweel and F. Scarano, "Universal outlier detection for PIV data," Exp. Fluids **39**, 1096–1100 (2005).

[60] A. Schiacchitano and B. Wieneke, "PIV uncertainty propagation," Meas. Sci. Technol. **27**, 084006 (2016).

[61] T. Janke and D. Michaelis, "Uncertainty quantification for PTV/LPT data and adaptive track filtering," in *14th International Symposium on Particle Image Velocimetry* (ISPIV, 2021), Vol. 1.

[62] R. L. Panton and J. M. Miller, "Excitation of a Helmholtz resonator by a turbulent boundary layer," J. Acoust. Soc. Am. **58**, 800–806 (1975).

[63] O. Marxen, M. Lang, U. Rist, O. Levin, and D. S. Henningson, "Mechanisms for spatial steady three-dimensional disturbance growth in a non-parallel and separating boundary layer," J. Fluid Mech. **634**, 165–189 (2009).